

Research  
Applied Geophysics—Article

## Quantitative Investigation of Tomographic Effects in Abnormal Regions of Complex Structures



Longjun Dong, Xiaojie Tong, Ju Ma \*

School of Resources and Safety Engineering, Central South University, Changsha 410083, China

### ARTICLE INFO

*Article history:*

Received 5 March 2020

Revised 30 April 2020

Accepted 10 June 2020

Available online 17 October 2020

*Keywords:*

Detection of abnormal regions

Tomographic effects

Wave velocity

Ray path

### ABSTRACT

The detection of abnormal regions in complex structures is one of the most challenging targets for underground space engineering. Natural or artificial geologic variations reduce the effectiveness of conventional exploration methods. With the emergence of real-time monitoring, seismic wave velocity tomography allows the detection and imaging of abnormal regions to be accurate, intuitive, and quantitative. Since tomographic results are affected by multiple factors in practical small-scale applications, it is necessary to quantitatively investigate those influences. We adopted an improved three-dimensional (3D) tomography method combining passive acoustic emission acquisition and active ultrasonic measurements. By varying individual parameters (i.e., prior model, sensor configuration, ray coverage, event distributions, and event location errors), 37 comparative tests were conducted. The quantitative impact of different factors was obtained. Synthetic experiments showed that the method could effectively adapt to complex structures. The optimal input parameters based on quantization results can significantly improve the detection reliability in abnormal regions.

© 2020 THE AUTHORS. Published by Elsevier LTD on behalf of Chinese Academy of Engineering and Higher Education Press Limited Company. This is an open access article under the CC BY license (<http://creativecommons.org/licenses/by/4.0/>).

### 1. Introduction

Underground construction has started attracting increasing attention with the gradual depletion of land space. However, the complex geological environment brings great challenges to urban underground transportation and tunnel construction projects. Various underground disasters, such as water inrush, mud surge, and roof collapse, can occur [1–5], causing huge risks to facilities and personnel [6–9].

Geophysical prospecting methods used in underground engineering are commonly classified into two categories: seismic and electromagnetic methods [10–19]. Seismic approaches, including advanced seismic prediction, scattering seismic computer tomography imaging, true reflection tomography, and land sonar [10–15], mainly analyze the propagation characteristics of elastic waves in geological bodies, and infer their distribution, geometric morphology, and structural characteristics [10–18]. Electromagnetic approaches, such as the ground penetrating radar and the transient electromagnetic methods, generally deduce the characteristics of a geological body through difference in the dielectric

constant and resistivity [14]. Both approaches can indirectly predict the existence of abnormal structures (e.g., water-rich areas) on a large scale.

With the emergence of new information technology like the Internet of Things, acoustic emission (AE) technology has been applied to the dynamic nondestructive testing of materials. It is mainly used in crack detection and fatigue fracture monitoring. AE technology can evaluate the integrity of components and the danger level of structures. Therefore, it has aroused great attention and gained rapid development in aviation, metallurgy, transportation, construction, and other fields. Based on the AE arrival time and other data, the source location and velocity structure can be iteratively solved. The inversion of the wave velocity field in the detected region defines abnormal (e.g., water-bearing) regions more intuitively, quickly, and accurately [20–26].

Jansen et al. [27] conducted ultrasonic imaging and AE monitoring for thermally induced microcracks in granite. Their study showed that both AE locations and slowness difference tomography clearly delineated the fracture plan. Nishizawa and Lei [28] employed the extended information criterion to advance the research on velocity tomography. Their meter-scale experiment revealed that this method provides an objective criterion for the selection of an optimum tomography solution. On a smaller scale, Lei and Xue [29] measured the ultrasonic velocity and attenuation

\* Corresponding author.

E-mail address: [majcsu@csu.edu.cn](mailto:majcsu@csu.edu.cn) (J. Ma).

during CO<sub>2</sub> injection into water-saturated porous sandstone using difference seismic tomography. They concluded that viscous losses due to fluid diffusion are of significant importance for compressional waves traveling at ultrasonic frequencies in porous rocks. Recently, Aben et al. [24] studied rupture energetics in crustal rock with laboratory-scale seismic tomography, in which a quasi-static rock fracture experiment combined with a novel seismic tomography method quantified the contribution of off-fault fracturing to the energy budget of a rupture.

In this paper, an improved three-dimensional (3D) AE tomography method based on the fast marching algorithm and least square quasi-Newton iteration is adopted to detect potential abnormal areas. This method is used for a joint inversion to obtain the 3D anisotropic P-wave structure using synthetic source locations and arrivals. By changing individual parameters, including the prior model, sensor configuration, inner event, origin model, ray coverage, and events location error, we explored the influence of different factors on imaging results.

## 2. Methods

In the synthetic experiment, through fast marching and standard optimization, the 3D anisotropic wave velocity imaging was conducted by combining active ultrasonic measurements with passive AE monitoring [30]. The inversion procedure is shown in Fig. 1. The improved algorithm contains the following five running steps: ① determining the initial environment and dividing mesh nodes; ② configuring the prior model; ③ collecting the required AE and

ultrasonic data; ④ executing tomography calculations and establishing the velocity structure database; and ⑤ identifying abnormal regions from the tomography results. The inversion procedure is shown in Fig. 1.

(1) Determining the initial environment. First, we determine the size of the area to be tomographically measured. The size of the unit grid cube can be decided based on the condition of the structure and requirement for tomography precision. Generally, the denser the grid is, the higher the tomography precision will be; correspondingly, more computation is needed, and the processing requires more time. However, when mesh density is high enough, tomography precision does not improve significantly with further mesh refinement. The matrix  $M$  of the same size as the grid node is established, and the index position  $(i, j, k)$  in the matrix corresponds one-to-one to the grid node position. The grid nodes form a collection that is used as starting points in the search for the fastest waveform path between subsequent nodes. It is assumed that the propagation velocity of the P wave in the surrounding normal region is an unknown value, which is represented by  $V$ .

(2) Configuring the prior model. The prior model is configured based on the characteristics of the structure. Abnormal regions in complex structures are not known in practical applications. As a result, we have to infer the information of the unknown origin model by iterative calculation, and finally conclude the approximate model. In this simulation test, the complex structure was simulated as granite, and the abnormal area was the paste-filling area. In general, the P-wave velocities of granite and paste-filling are 4000 to 5500 and 1500 m·s<sup>-1</sup>, respectively. Therefore, in the synthetic tests, the true model was set at 4500 and 1500 m·s<sup>-1</sup>

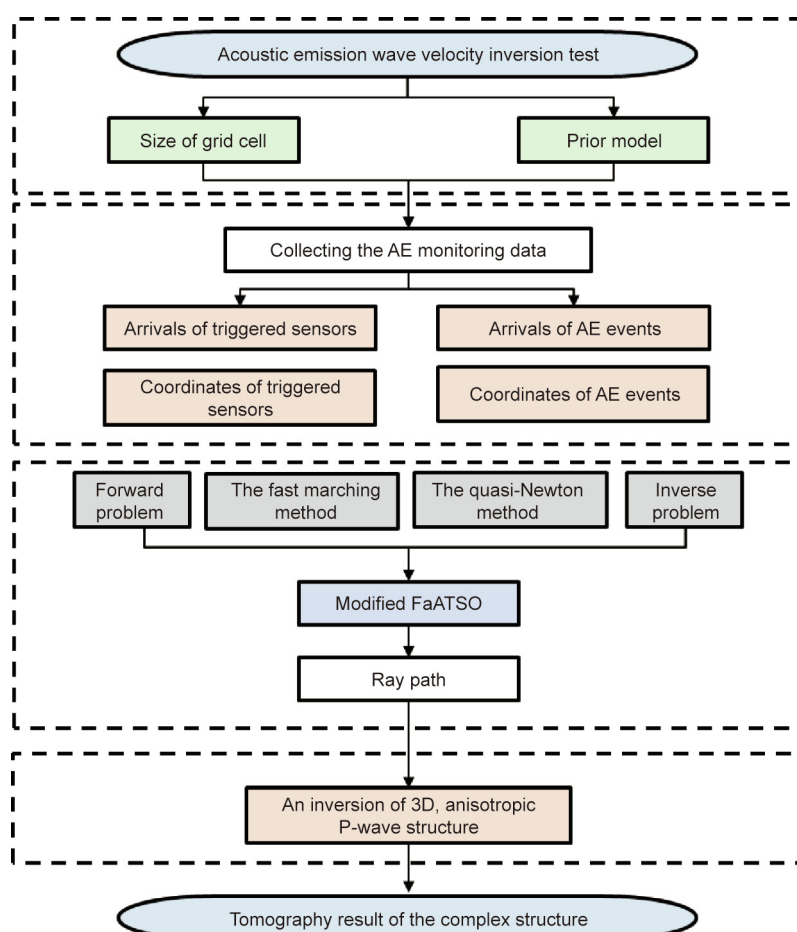


**Fig. 1.** Flowchart of the inversion algorithm. FaATSO: fast marching acoustic emission tomography using standard optimization.

for granite (external region) and paste-filling (internal region), respectively. The average of the internal and external wave velocities was taken as the prior model.

(3) Collecting AE and ultrasonic data. Sensors, which are capable of actively transmitting and receiving the AE signal, were installed at different positions of the structure to be tested. In the 3D model, there are five source parameters (i.e., P-wave velocity  $V$ , AE source coordinate  $(x_0, y_0, z_0)$ , and initial excitation time  $t_0$ ). Therefore, the sensor number  $m$  must be an integer no less than 5. The sensor transmitting pulse signal is the active source  $S_i$ , whose coordinate and transmitting time are  $(x_i, y_i, z_i)$  and  $t_0^i$ , respectively. For the  $k$ th sensor  $S_k$  that receives the AE signal, the coordinate is  $(x_k, y_k, z_k)$ , and the initial arrival time of the P-wave AE signal is  $t_0^k$ . For an unknown source  $P_0$  with position coordinates of  $(x_0, y_0, z_0)$ , its initial excitation time is  $t_0$ .

$$\Delta t_0^{ik} = t_0^k - t_0 \quad (1)$$

$$\Delta t_0^k = t_0 - t_0^k \quad (2)$$

where  $\Delta t_0^{ik}$  represents the difference of the actual arrival time between sensors  $S_i$  and  $S_k$ , while  $\Delta t_0^k$  is the actual arrival time difference between  $P_0$  and  $S_k$ .

In this study, the coordinates of sensors and AE events (rough locations), as well as the arrival time differences of the sources, are all input data.

The P-wave velocity of each grid point in the structure was obtained by iterative calculation. These values were represented by different colors in the 3D diagram; the ray paths of the active sources and AE events to the receiving sensor were marked at the same time. Therefore, the boundary and location of the abnormal region in the complex structure can be intuitively separated via color difference. In addition, the properties of the abnormal region can be analyzed based on P-wave velocity values.

### 3. Experiment

In an assumed  $100 \text{ mm} \times 100 \text{ mm} \times 100 \text{ mm}$  cube with a  $60 \text{ mm}$  (diameter) through-hole in the center, seven sensors were evenly arranged on each of the four vertical sides of the cube. In particular, when analyzing the influence of sensor arrangement on tomography results, another four sensors were uniformly distributed in the circular hole on the upper and lower surfaces of the cube. Sensors in synthetic tests have the active transmitted pulse function. Therefore, they can not only be used as the active AE source but also as receivers. Six hundred AE events were randomly generated inside the cube: 170 and 430 AE events inside and outside the internal hole area, respectively. The exact coordinate of each AE event was known and each event could be detected by every sensor.

The through-hole simulating the abnormal region in practical applications is hereinafter referred to as “internal,” and its P-wave velocity is represented by  $V_{\text{in}}$ ; the structure outside the hole is referred to as “external,” and its P-wave velocity is represented by  $V_{\text{out}}$ . In synthetic tests, granite and paste-filling were considered to be the medium of the external and internal regions,

respectively. To study the influence of different factors on tomography results, we quantitatively tested the prior model, sensor configuration, event distribution, origin model, ray coverage, and event location errors.

After calculating the tomography results of each synthetic experiment and obtaining the ray paths, we compared the inversion P-wave velocity  $V_t$  of each grid node with the actual value  $V_o$  of the origin model. If the difference between them is less than  $\pm 20\%$ , the tomography result is regarded as valid. To quantitatively represent the effects of various influencing factors on inversion results,  $V_t$  of each grid in an experiment was compared with its corresponding  $V_o$  to calculate the tomography result accuracy under a specific condition.

## 4. Results and discussion

### 4.1. Prior model and sensor configuration

To evaluate the influence of the prior model and sensor arrangement on tomographic effects, two groups of four tests were conducted (Table 1). In addition to the 28 sensors placed around the cube, we placed four sensors above the through-hole area in Test3 and added another four sensors below the through-hole area in Test4. Test1 was compared with Test2 to analyze the influence of the prior model; Tests2, 3, and 4 were compared to investigate the effect of sensor configuration. In this scenario, the 170 AE events inside the through-hole area were eliminated, while the 430 events outside the through-hole area were retained. That is, there were no AE events inside the anomalous area.

Before tomography inversions, we prepared the time arrivals of active ultrasonic measurements and AE events. The imaging results are shown in Fig. 2. Five tangent planes perpendicular to the  $z$ -axis represent the tomography results of the 3D P-wave velocity (Fig. 2). Propagation paths from the active pulse to the receiving sensor are shown as blue curves, and the ray paths of the AE event are presented by orange curves (one AE event was chosen randomly). Quantitative analysis of the P-wave velocity is shown in Fig. 3.

As shown in the tomographic results (Fig. 2), Fig. 2(a) presents a perfect  $\phi 60 \text{ mm}$  circle; in Figs. 2(a)–(d), the circle disappeared. Moreover, when comparing the three tests in Group2, changing the sensor configuration did not work. Even when the sensor was placed on the paste-filling surface, the rays still bypassed the paste-filling area and passed through the rock. According to the tomographic results, relatively higher accuracies were obtained in the upper and lower sections of the structure. This is because the ultrasonic pulse signals of sensors arranged at the top and bottom of the hole bypassed the inside area and travelled through the outside in the upper and lower sections.

For Group1, when the prior model was equal to the origin model and the velocity precision was limited to 20%, the inverted  $V_{\text{out}}$  and  $V_{\text{in}}$  was 100% correct (Fig. 3). For the three tests in Group2, when the prior model was different from the origin model, the correct rate of  $V_{\text{in}}$  was less than 5% (Fig. 3), indicating that the abnormal velocity area cannot be accurately identified; however, the  $V_{\text{out}}$  still had relatively high accuracy.

**Table 1**

Configurations of the model and sensor layout.

Group	Test	Origin model $V_{\text{out}}/V_{\text{in}}$	Prior model $V_{\text{out}}/V_{\text{in}}$	Sensor configuration
Group1	Test1	4.5/1.5	4.5/1.5	28
Group2	Test2	4.5/1.5	3.0/3.0	28
	Test3	4.5/1.5	3.0/3.0	28 + 4 up
	Test4	4.5/1.5	3.0/3.0	28 + 4 up + 4 down

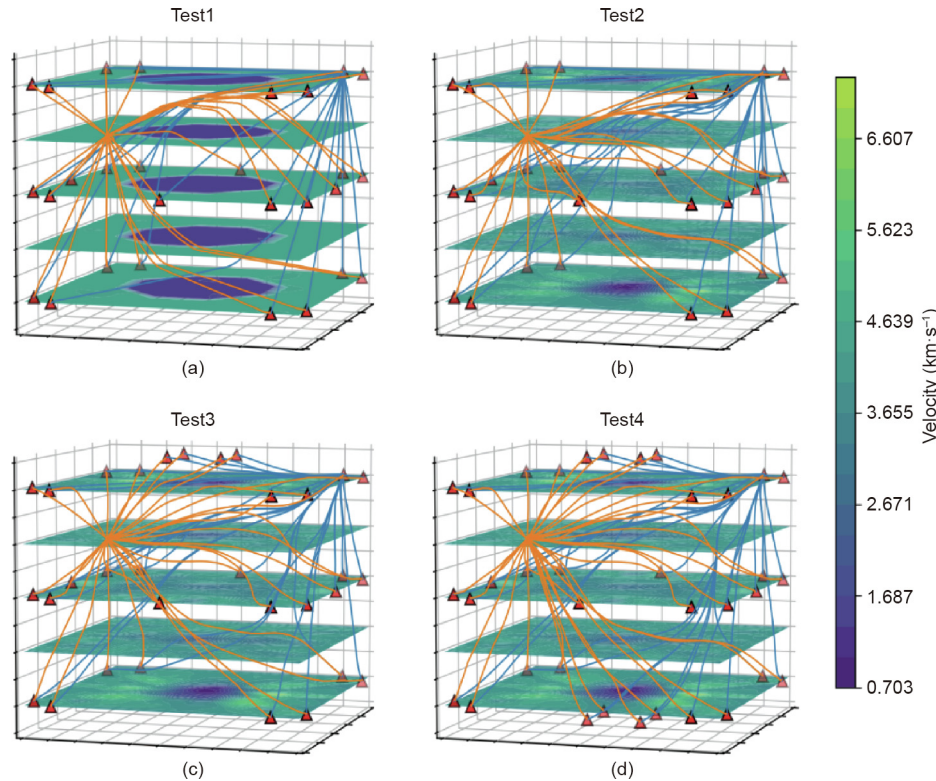


**Fig. 2.** Inversion results with different models and sensor layouts.

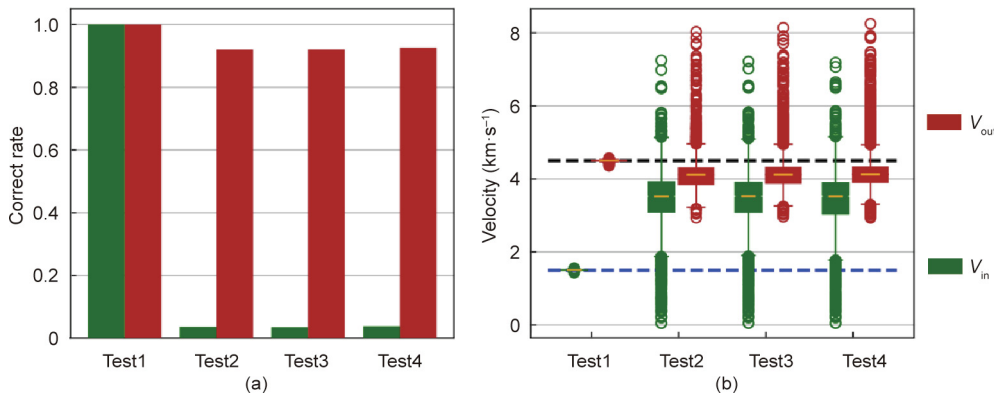


**Fig. 3.** Quantitative influences of the model and sensor arrangement. (a) Correct rate for the  $V_{in}$  and  $V_{out}$ ; (b) velocity distribution for the  $V_{in}$  and  $V_{out}$ .

#### 4.2. Events distribution

Results in the previous section indicate that when the prior model is not close to the realistic case, the internal P-wave velocity values are calculated by iterative calculations based on input parameters. However, these results are not satisfying. The fact that the ray path of external events may not bypass the inside area could be one of the reasons affecting the tomographic effects. To examine whether this conjecture is true, i.e., whether there are

differences in tomographic results in the presence and absence of internal events, the 170 inner events were added to the tests. We set another three tests corresponding to Tests2, 3, and 4 in Group2. Except for the 170 AE events located in the abnormal region (the through-hole area), all parameters remained unchanged (Table 2).

The test results are shown in Figs. 4 and 5. Different from sensors on the paste-filling surface, rays from inner events had to pass through the paste-filling area. However, the results were consistent with the previous ones, indicating that adding inner events

**Table 2**

Parameters of influencing factors with inner events.

Group	Test	Origin model $V_{out}/V_{in}$	Prior model $V_{out}/V_{in}$	Sensor configuration	Inner events
Group3	Test1	4.5/1.5	3.0/3.0	28	170
	Test2	4.5/1.5	3.0/3.0	28 + 4 up	—
	Test3	4.5/1.5	3.0/3.0	28 + 4 up + 4 down	—

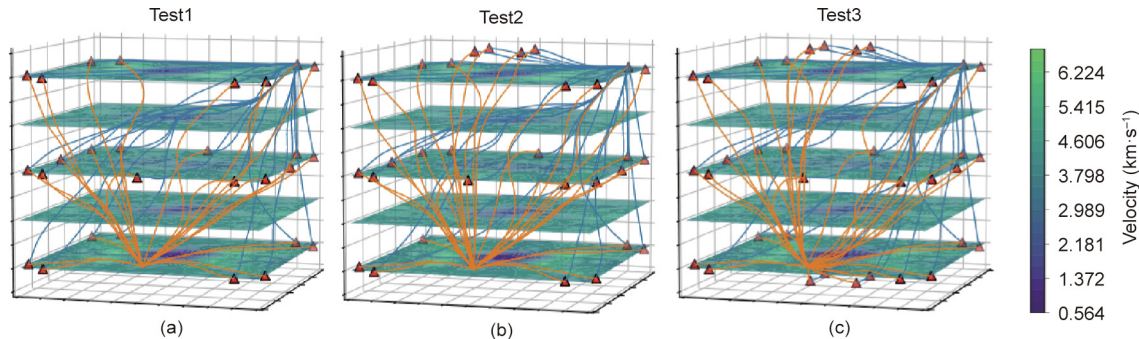


**Fig. 4.** Inversion results with different sensor layouts in the presence of inner events. (a) With 28 surrounding sensors; (b) with 28 surrounding sensors and 4 top sensors; (c) with 28 surrounding sensors, 4 top sensors, and 4 bottom sensors.

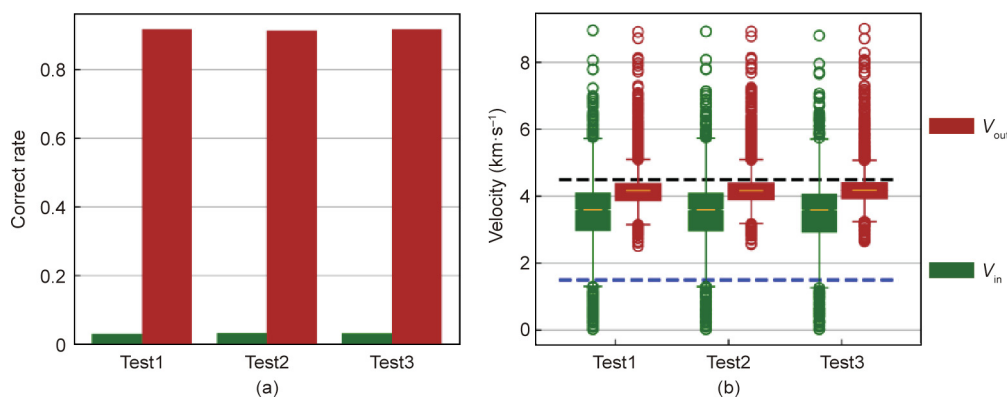


**Fig. 5.** Quantitative influences of the sensor arrangement in the presence of inner events. (a) Correct rate for the  $V_{\text{in}}$  and  $V_{\text{out}}$ ; (b) velocity distribution for the  $V_{\text{in}}$  and  $V_{\text{out}}$ .

did not improve the tomographic effects when the origin model  $V_{\text{out}}/V_{\text{in}}$  equaled 4.5/1.5.

Tomographic effects obtained in the above experiments suggest that when the actual P-wave velocities in the external and internal (abnormal) regions were 4.5 and 1.5 km·s<sup>-1</sup>, respectively, and the input  $V_{\text{out}} = V_{\text{in}} = 3$  km·s<sup>-1</sup> in the prior model, the inversion accuracy of the abnormal area was lower than 5%. Since the deviation of 20% is recognized as correct, changing the sensor layout or increasing the number of AE events in the abnormal region was almost ineffective.

#### 4.3. Origin model

We further analyzed the effects of the origin model and the prior model on tomography results. In the new tests,  $V_{\text{out}}/V_{\text{in}}$  in the origin model varies from 4.5/1.5 to 4.5/4.0. The prior model used the average of  $V_{\text{out}}$  and  $V_{\text{in}}$ . There were no AE events in the abnormal region. The experiment configurations are listed in Table 3.

The tomographic results (Fig. 6) and the correct rate (Fig. 7) suggest that the inversion result was better when the difference

between  $V_{\text{out}}$  and  $V_{\text{in}}$  was smaller (i.e.,  $V_{\text{out}}/V_{\text{in}}$  was closer to 1). Especially, for Tests 5 and 6, the accuracies of  $V_{\text{out}}$  and  $V_{\text{in}}$  reached almost 100%. Fig. 6 also shows that the ray paths of Tests 5 and 6 are less curved or nearly straight.

We narrowed the accepted velocity precision tolerance from 20% to 15% and finally to 1%. As shown in Fig. 8, the correct rates of  $V_{\text{out}}$  and  $V_{\text{in}}$  exceeded 50% in Tests 5 and 6 when the precision tolerance was limited to 5% and 1%, respectively. When  $V_{\text{out}}/V_{\text{in}}$  was 4.5/4.0 or 4.5/3.5, namely  $(V_{\text{out}} - V_{\text{in}})/V_{\text{out}}$  was less than 25%, the inversion results were very good despite there being only 28 sensors and the absence of inner events.

As the difference between  $V_{\text{out}}$  and  $V_{\text{in}}$  gradually increased, the inversion accuracy of  $V_{\text{in}}$  decreased. However, as shown in the path diagram of Tests 2, 3, and 4, the  $V_{\text{in}}$  (abnormal) area still could be distinguished (Fig. 6). The ray paths were tortuous and the internal area could not be detected when  $V_{\text{out}}$  and  $V_{\text{in}}$  were 4.5 and 1.5 km·s<sup>-1</sup>, respectively.

Since the correct rate changes with the difference between  $V_{\text{out}}$  and  $V_{\text{in}}$ , we define the index  $E$  as

$$E = \frac{|V_{\text{out}} - V_{\text{in}}|}{V_{\text{out}}} = \frac{\Delta V}{V_{\text{out}}} \quad (3)$$

The inversion results corresponding to different  $E$  values from the above synthetic experiments are shown in Table 4.

Among the four influencing factors—prior model, origin model, sensor configuration, and inner events—the origin model plays a decisive role in determining the tomographic results. When  $V_{\text{out}}/V_{\text{in}}$  in the origin model was 4.5/1.5, the tomographic results were not satisfying; the changes in the layout of sensors and the increase in inner events did not improve the tomography results. When the index  $E$  is higher than 50%, the results are not reliable;

**Table 3**

Parameters of influencing factors with origin and prior models.

Test	Origin model $V_{\text{out}}/V_{\text{in}}$	Prior model $V_{\text{out}}/V_{\text{in}}$	Sensor configuration
Test1	4.5/1.5	3.00/3.00	28
Test2	4.5/2.0	3.25/3.25	28
Test3	4.5/2.5	3.50/3.50	28
Test4	4.5/3.0	3.75/3.75	28
Test5	4.5/3.5	4.00/4.00	28
Test6	4.5/4.0	4.25/4.25	28

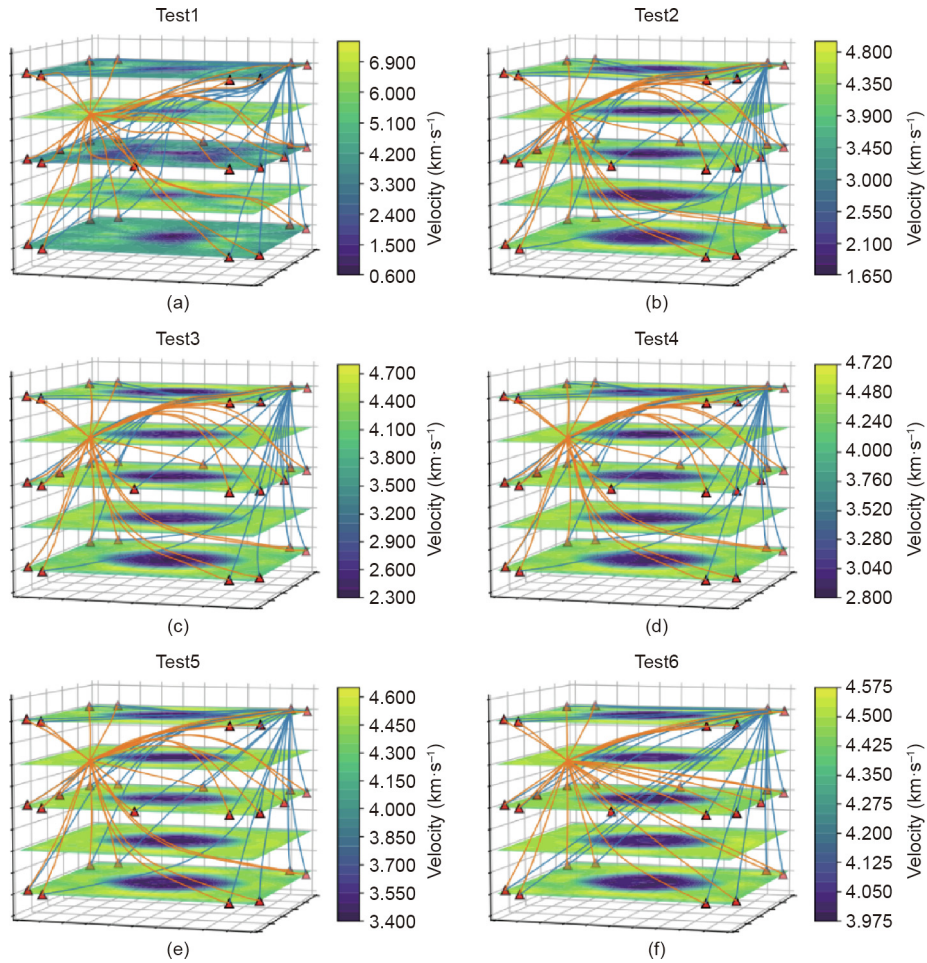


**Fig. 6.** Inversion results with different origin and prior models. (a) The origin velocity for  $V_{\text{out}}$  is  $4.5 \text{ km}\cdot\text{s}^{-1}$  and  $V_{\text{in}}$  is  $1.5 \text{ km}\cdot\text{s}^{-1}$ , the prior velocities for  $V_{\text{out}}$  and  $V_{\text{in}}$  are both  $3.0 \text{ km}\cdot\text{s}^{-1}$ ; (b) the origin velocity for  $V_{\text{out}}$  is  $4.5 \text{ km}\cdot\text{s}^{-1}$  and  $V_{\text{in}}$  is  $2.0 \text{ km}\cdot\text{s}^{-1}$ , the prior velocities for  $V_{\text{out}}$  and  $V_{\text{in}}$  are both  $3.25 \text{ km}\cdot\text{s}^{-1}$ ; (c) the origin velocity for  $V_{\text{out}}$  is  $4.5 \text{ km}\cdot\text{s}^{-1}$  and  $V_{\text{in}}$  is  $2.5 \text{ km}\cdot\text{s}^{-1}$ , the prior velocities for  $V_{\text{out}}$  and  $V_{\text{in}}$  are both  $3.5 \text{ km}\cdot\text{s}^{-1}$ ; (d) the origin velocity for  $V_{\text{out}}$  is  $4.5 \text{ km}\cdot\text{s}^{-1}$  and  $V_{\text{in}}$  is  $3.0 \text{ km}\cdot\text{s}^{-1}$ , the prior velocities for  $V_{\text{out}}$  and  $V_{\text{in}}$  are both  $3.75 \text{ km}\cdot\text{s}^{-1}$ ; (e) the origin velocity for  $V_{\text{out}}$  is  $4.5 \text{ km}\cdot\text{s}^{-1}$  and  $V_{\text{in}}$  is  $3.5 \text{ km}\cdot\text{s}^{-1}$ , the prior velocities for  $V_{\text{out}}$  and  $V_{\text{in}}$  are both  $4.0 \text{ km}\cdot\text{s}^{-1}$ ; (f) the origin velocity for  $V_{\text{out}}$  is  $4.5 \text{ km}\cdot\text{s}^{-1}$  and  $V_{\text{in}}$  is  $4.0 \text{ km}\cdot\text{s}^{-1}$ , the prior velocities for  $V_{\text{out}}$  and  $V_{\text{in}}$  are both  $4.25 \text{ km}\cdot\text{s}^{-1}$ .

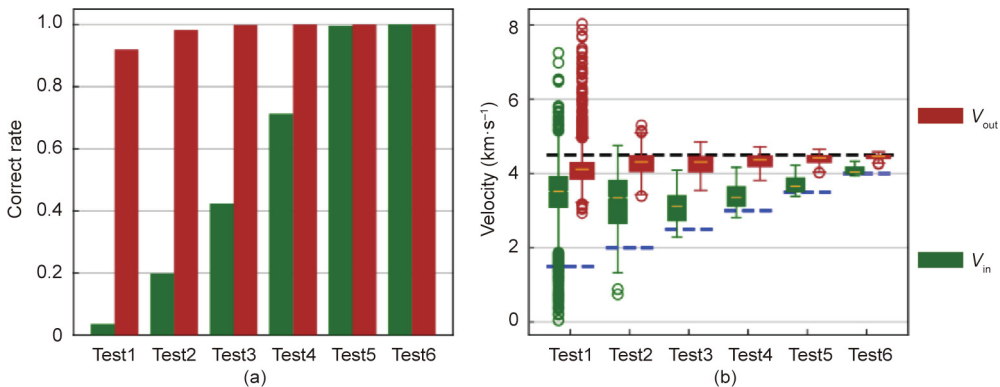


**Fig. 7.** Quantitative influences of the origin and prior models. (a) Correct rate for the  $V_{\text{in}}$  and  $V_{\text{out}}$  (values with 20% deviation are recognized as correct); (b) velocity distribution for the the  $V_{\text{in}}$  and  $V_{\text{out}}$ .

when  $E$  is between 25% and 50%, the results are reliable and stable; and when  $E$  is lower than 25%, the results are of relatively high accuracy. In addition, the accuracy of  $V_{\text{in}}$  in the upper and lower sections, as well as that of  $V_{\text{out}}$ , are relatively high, even though the tomography results are poor on the whole.

#### 4.4. Ray coverage

When the difference between the internal and external P-wave velocities was too large, the methods used failed to improve the results. The ray path of the P-wave changes in different media. A

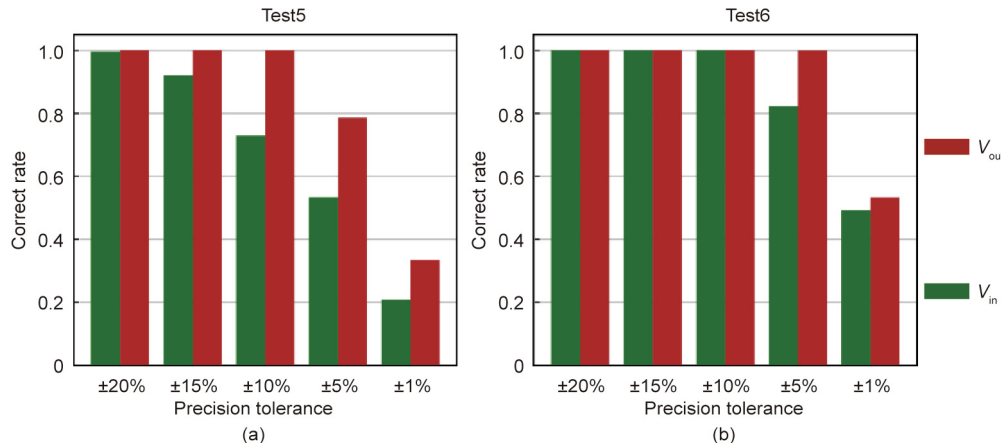


**Fig. 8.** Quantitative influences of the origin and prior models for Tests5 and 6 with different precision tolerances.

**Table 4**

E index and inversion effect corresponding to different origin models.

Test	Origin model $V_{\text{out}}/V_{\text{in}}$	E (%)	Correct rate	Tomography effect
Test1	4.5/1.5	66.7%	< 5%	★
Test2	4.5/2.0	55.6%	20%	★
Test3	4.5/2.5	44.4%	42%	★★
Test4	4.5/3.0	33.3%	70%	★★★
Test5	4.5/3.5	22.2%	≈ 100%	★★★★★
Test6	4.5/4.0	11.1%	≈ 100%	★★★★★

The tomography effects are intuitively presented by the increasing number of stars. The more stars the higher correct rate.

greater difference in the medium led to a more complex propagation mechanism and lower inversion accuracy, which is a common limitation of current AE wave velocity tomographic inversion methods [30].

Six additional tests (Table 5) were conducted in the synthetic structure. No AE events were generated inside the abnormal region, while AE events increased from 0 to 400 outside the abnormal region. The precision tolerance between the inverted P-wave velocity and the actual value was limited to  $\pm 5\%$ . The results are shown in Figs. 9 and 10.

The identification accuracy of the internal abnormal region increased with more outer AE events from Tests1 to 6 (Fig. 9). In addition, the  $V_{\text{in}}$  accuracy increased with AE events while the  $V_{\text{out}}$  accuracy remained relatively high (Fig. 10).

The above analysis indicates that when the origin model has a high inversion accuracy range, increasing ray coverage (by increasing the number of external AE events) can improve inversion accuracy. However, as the event number increases, the increasing rate

of inversion accuracy tends to be flat (Fig. 10), meaning that it is difficult to significantly improve the correct rate by infinitely increasing the AE event number. As a result, a suitable number or range of AE events should be determined, so that a higher accuracy with a relatively small number of AE events can be obtained to save the cost in practical applications.

#### 4.5. Event location error

In synthetic tests, events were automatically generated, and their locations were therefore precisely known. However, the location of an AE event is unknown in practical applications. At present, there are multiple AE location methods [4,7–9]. Methods without pre-measured wave velocity greatly reduce the location error [7]. Nevertheless, there is still an error between the location results and the actual positions. Consequently, it is imperative to understand how the magnitude of the location error affects the inversion results.

We investigated the effect of AE event location errors on tomographic inversion in two schemes, in which the number of external AE events was 400. In the first scheme (Scheme 1), all AE events had errors and the allowed location varying range expanded from  $(0.95, 1.05)$  to  $(0.75, 1.25)$ , that is, the location error increase from  $\pm 5\%$  to  $\pm 25\%$  at the interval of 5%. In the second scheme (Scheme 2), the location error is fixed at  $\pm 20\%$  and the number of mis-locating events increased from 50 to 300 at the interval of 50; the other conditions were the same as in Scheme 1. The configurations for Schemes 1 and 2 are listed in Tables 6 and 7, respectively. The results are shown in Figs. 11–14.

The inversion results of Scheme 1 are shown in Fig. 11. From Tests1 to 6, the error range increased from  $\pm 5\%$  to  $\pm 25\%$ , and the tomographic effects became worse. For Test3, where the error range was  $\pm 10\%$ , the cylindrical P-wave velocity of the abnormal region in the center could still be observed. When the error reached  $\pm 15\%$  or more (i.e., in Tests4, 5, and 6), according to the

**Table 5**

Parameters of influencing factors with ray coverage.

Test	Origin model $V_{\text{out}}/V_{\text{in}}$	Prior model $V_{\text{out}}/V_{\text{in}}$	Ray coverage
Test1	4.5/4.0	4.25/4.25	Only active ultrasonic measurements
Test2	4.5/4.0	4.25/4.25	Ultrasonic measurements + 50 AE events
Test3	4.5/4.0	4.25/4.25	Ultrasonic measurements + 100 AE events
Test4	4.5/4.0	4.25/4.25	Ultrasonic measurements + 200 AE events
Test5	4.5/4.0	4.25/4.25	Ultrasonic measurements + 300 AE events
Test6	4.5/4.0	4.25/4.25	Ultrasonic measurements + 400 AE events

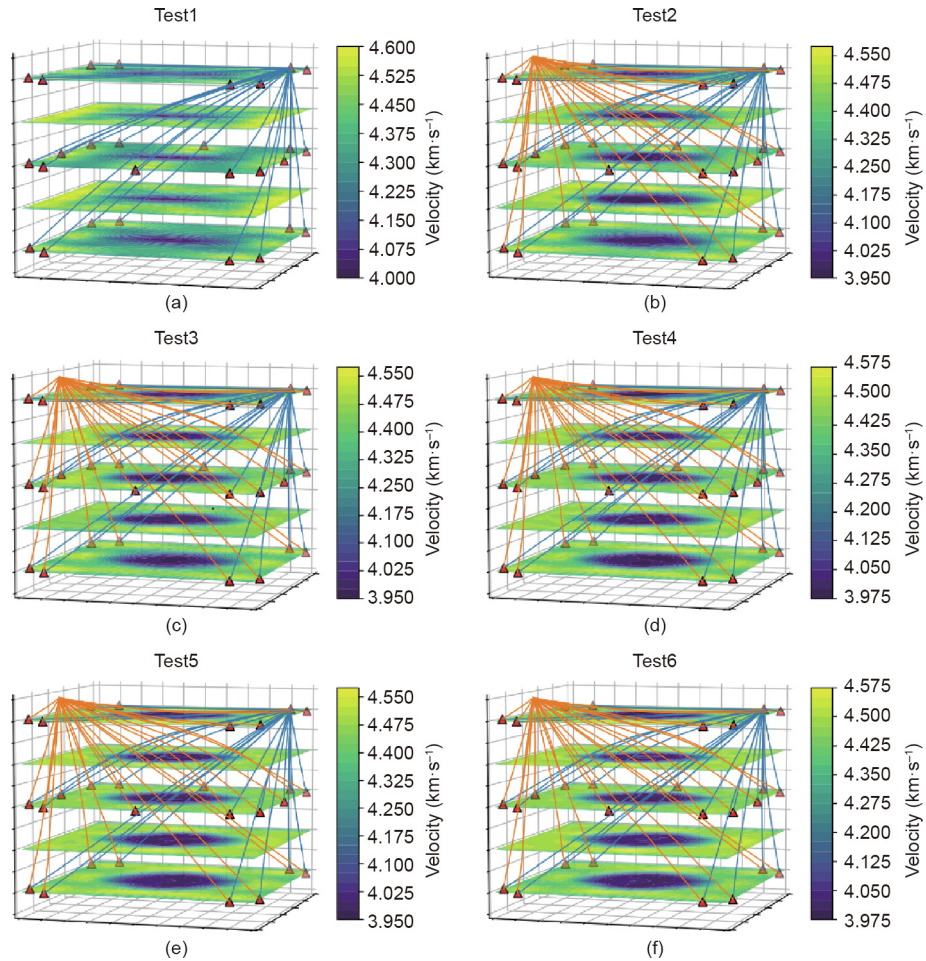


**Fig. 9.** Inversion results with different ray coverage. (a) With only active ultrasonic measurements rays; (b) with ultrasonic measurements rays and 50 event rays; (c) with ultrasonic measurements rays and 100 event rays; (d) with ultrasonic measurements rays and 200 event rays; (e) with ultrasonic measurements rays and 300 event rays; (f) with ultrasonic measurements rays and 400 event rays.

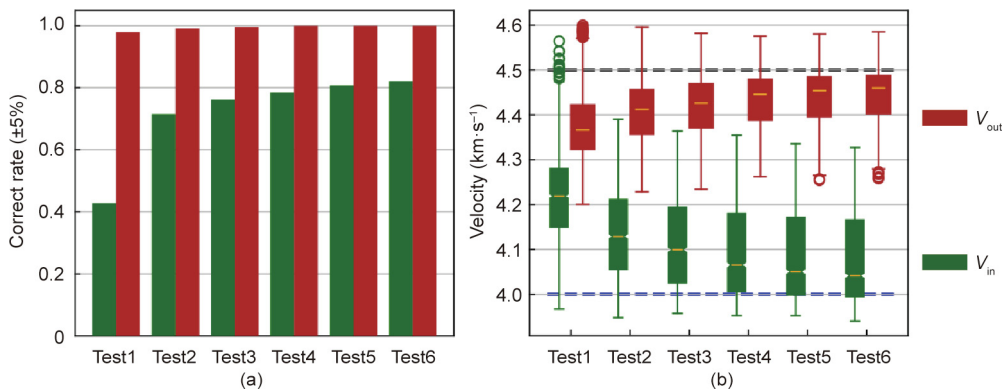


**Fig. 10.** Quantitative influences of the ray coverage. (a) Correct rate for the  $V_{in}$  and  $V_{out}$  (values with 5% deviation are recognized as correct); (b) velocity distribution for the  $V_{in}$  and  $V_{out}$ .

**Table 6**

Parameters of influencing factors with event location errors.

Test	Origin model $V_{out}/V_{in}$	Prior model $V_{out}/V_{in}$	Event location noise on $x/y/z$
Test1	4.5/4.0	4.25/4.25	0.00
Test2	4.5/4.0	4.25/4.25	Random (0.95, 1.05)
Test3	4.5/4.0	4.25/4.25	Random (0.90, 1.10)
Test4	4.5/4.0	4.25/4.25	Random (0.85, 1.15)
Test5	4.5/4.0	4.25/4.25	Random (0.80, 1.20)
Test6	4.5/4.0	4.25/4.25	Random (0.75, 1.25)

inversion diagram, the internal and external P-wave velocity values increased, the boundaries of the internal and external wave velocity became blurred, and it was difficult to observe the abnormal region in the structure.

The quantified results of Scheme 1 (Fig. 12) show that the correct rate (5% deviation between the tomographic wave velocity and the actual value was recognized as correct) exceeded 70% when the location error was  $\pm 10\%$ . In real applications, the location error in AE experiments can be easily limited to 10% [7]; for a sample of 100 mm, the location error can be less than 10 mm. Therefore,

**Table 7**

Parameters of influencing factors with mis-locating events.

Test	Origin model $V_{\text{out}}/V_{\text{in}}$	Prior model $V_{\text{out}}/V_{\text{in}}$	Event location noise on x/y/z	Number of mis-locating events
Test1	4.5/4.0	4.25/4.25	0.00	50
Test2	4.5/4.0	4.25/4.25	Random (0, 0.2)	100
Test3	4.5/4.0	4.25/4.25	Random (0, 0.2)	150
Test4	4.5/4.0	4.25/4.25	Random (0, 0.2)	200
Test5	4.5/4.0	4.25/4.25	Random (0, 0.2)	250
Test6	4.5/4.0	4.25/4.25	Random (0, 0.2)	300

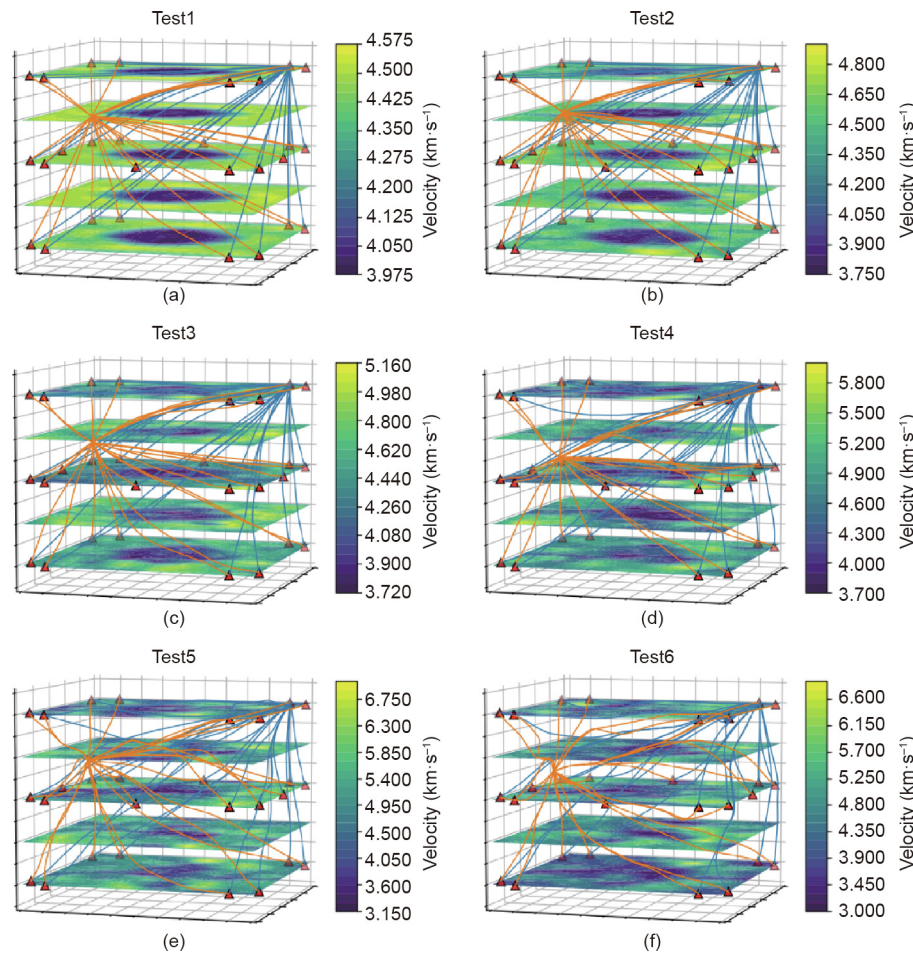


**Fig. 11.** Inversion results with different event location errors. (a) The event locations are without any error; (b) the event locations are scaled to 0.95–1.05 times of the true values; (c) the event locations are scaled to 0.90–1.10 times of the true values; (d) the event locations are scaled to 0.85–1.15 times of the true values; (e) the event locations are scaled to 0.80–1.20 times of the true values; (f) the event locations are scaled to 0.75–1.25 times of the true values.

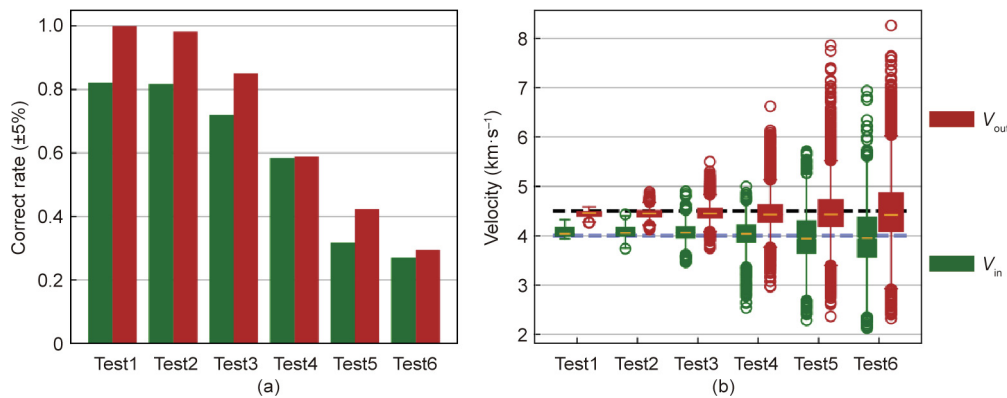


**Fig. 12.** Quantitative influences of the event location errors. (a) Correct rate for the  $V_{\text{in}}$  and  $V_{\text{out}}$ ; (b) velocity distribution for the  $V_{\text{in}}$  and  $V_{\text{out}}$ .

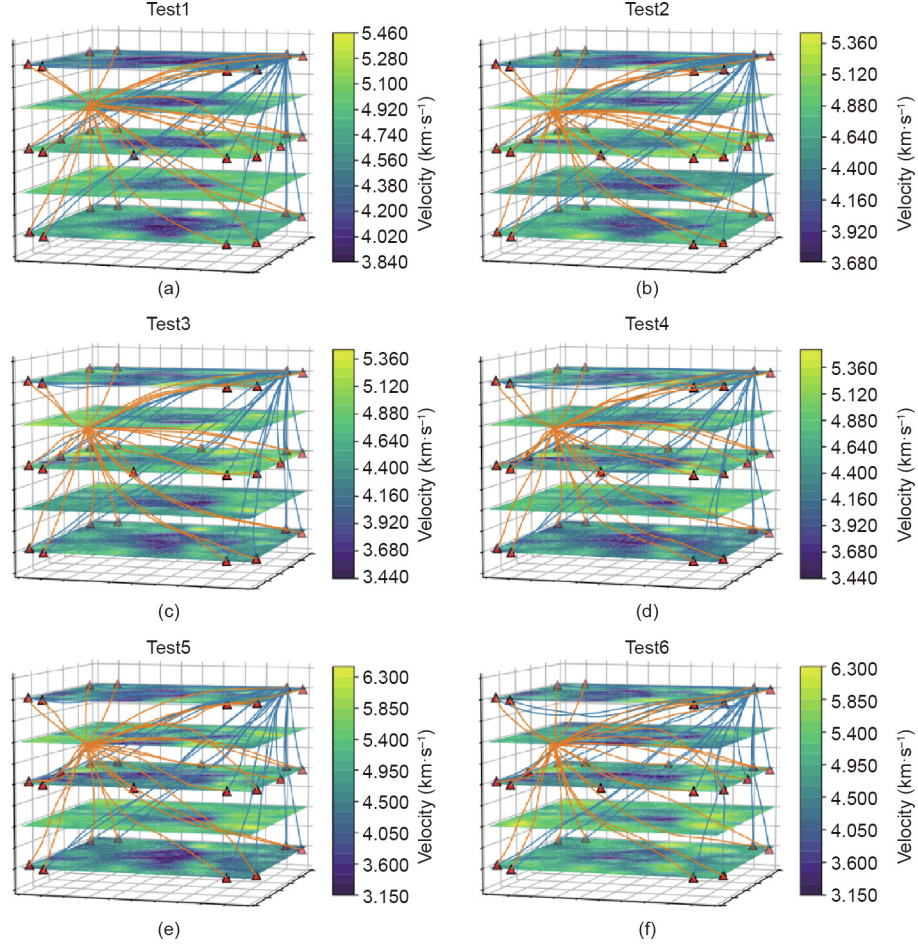


**Fig. 13.** Inversion results with a different number of mis-located events. (a) With 50 mis-locating events; (b) with 100 mis-locating events; (c) with 150 mis-locating events; (d) with 200 mis-locating events; (e) with 250 mis-locating events; (f) with 300 mis-locating events.

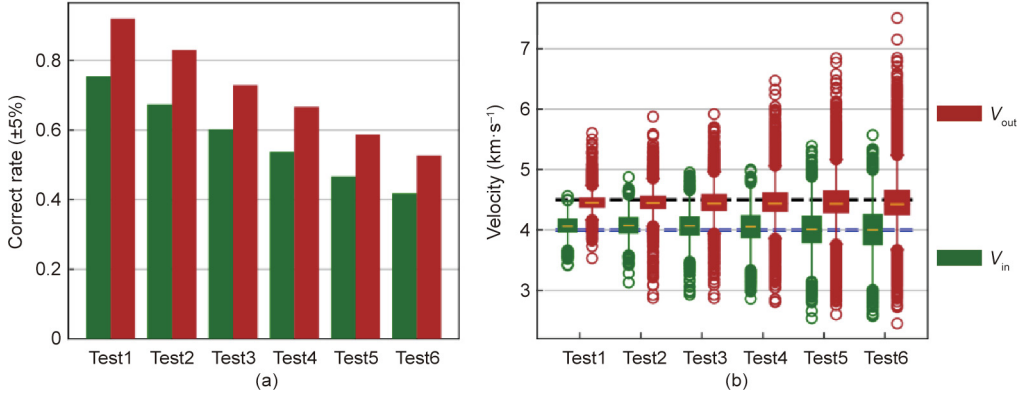


**Fig. 14.** Quantitative influences of the number of mis-located events. (a) Correct rate for the  $V_{in}$  and  $V_{out}$ ; (b) velocity distribution for the  $V_{in}$  and  $V_{out}$ .

the AE P-wave velocity tomography method can reliably inverse the size and range of the abnormal region in a complex structure in the origin model with  $V_{out}/V_{in}$  of 4.5/4.0 and a reasonable location error.

The inversion results of Scheme 2 are shown in Fig. 13. As the number of error events increased from 50 to 300, the inversion effect became worse. The quantitative analysis chart (Fig. 14) reveals that the correct rate decreased from Test1 to Test6, which was slower than that in Scheme 1.

The comparison with Test6 in Section 4.3 (i.e., the number of external events was 430, and the event location was correct) suggests that erroneous location data have a great impact on inversion results. When the allowable error of the correct rate was 5%, the number of AE events changed from 430 correct to 350 correct and 50 errors, the accuracy rates of  $V_{out}$  and  $V_{in}$  dropped from 100% to 95% and from 83% to 75%, respectively. When the number of errors in AE events increased to 300 (with 400 total events), the accuracies of  $V_{out}$  and  $V_{in}$  reduced to approximately 30%; the

inversion results were no longer reliable. Therefore, unreasonable, mis-located AE events affect the accuracy of tomographic inversion.

We noticed that in this synthetic experiment,  $V_{\text{out}}$  was always more correct than  $V_{\text{in}}$ . Due to the low wave velocity in the abnormal zone, rays bypass this area boundaries. Since very few rays pass through, there is a lack of ray data to calculate  $V_{\text{in}}$ , which ultimately results in less accurate results for  $V_{\text{in}}$ .

## 5. Conclusions

To analyze the influencing factors of AE wave velocity tomographic inversion, an improved 3D tomography method combining active and passive AE sources was adopted. A variety of comparative synthetic tests were performed, and quantitative analysis evaluated the influence of the following six factors: prior model, sensor configuration, inner events, origin model, ray coverage, and event location errors. The results show that optimal input parameters can significantly increase the tomography reliability of abnormal regions in complex structures.

Among the six influencing factors, the origin model plays a decisive role in the tomographic results. Therefore, if there is a big difference in P-wave velocity between the abnormal region and the surrounding region of the structure, it is difficult to achieve desirable results. The difference between the internal and external wave velocities is represented by the index  $E$ . In general, when  $E \geq 50\%$ , the inversion result is not reliable. In a future study, we will consider adding weights to the low-speed region when the  $E$  value is too high, to reduce the  $E$  value and then to restore the inversion result corresponding to the correct wave velocity value.

When  $E$  is in a reasonable range, an origin model with a relatively high tomography accuracy is expected. When the number of external AE events reduces, the inversion accuracy decreases; the accuracy improvement rate becomes slower with an increasing number of events. Therefore, the appropriate number of events corresponding to a higher accuracy rate should be determined, to suggest an optimal scheme for practical applications. The inversion accuracy is also influenced if location errors increase. An acceptable range of location errors can allow a satisfactory accuracy. At the same time, by screening AE events in practical experiments, eliminating unreasonable AE events can improve tomographic inversion.

The premise of this velocity imaging method is that the material needs to be transversely isotropic with a vertical axis of symmetry (VTI), whose phase velocity is completely determined by the phase angle. In practice, the assumption of VTI geometry is particularly relevant to initially isotropic rock samples subjected to triaxial compression in the laboratory. In addition, this method is not very suitable for cases with major differences in wave velocity within a structure. It is more reliable and stable for cases with slowly changing wave velocity. In this study, we only tested a cylindrical anomalous area. The actual situation is much more complicated, and the tomography accuracy may be different in cases with anomalous shapes. Since the prior model is important for the inversion and we cannot accurately estimate the model in advance, a two-step strategy is suggested for rock experiments. That is, the ultrasonic survey should be performed first to estimate the approximate velocity in the structure, which is thereafter used as the prior model for later AE tomography.

## Acknowledgements

The authors wish to acknowledge financial support from the National Natural Science Foundation of China (51822407, 51774327, and 51904334).

## Compliance with ethics guidelines

Longjun Dong, Xiaojie Tong, and Ju Ma declare that they have no conflict of interest or financial conflicts to disclose.

## References

- [1] Ma J, Dong LJ, Zhao GY, Li XB. Focal mechanism of mining-induced seismicity in fault zones: a case study of Yongshaba mine in China. *Rock Mech Rock Eng* 2019;52(9):3341–52.
- [2] Feng GL, Feng XT, Chen BR, Xiao YX, Liu GF, Zhang W, et al. Characteristics of microseismicity during breakthrough in deep tunnels: case study of Jinping-II Hydropower Station in China. *Int J Geomech* 2020;20(2):04019163.
- [3] Ma J, Dong LJ, Zhao GY, Li X. Discrimination of seismic sources in an underground mine using full waveform inversion. *Int J Rock Mech Min Sci* 2018;106:213–22.
- [4] Dong LJ, Zou W, Li XB, Shu WW, Wang ZW. Collaborative localization method using analytical and iterative solutions for microseismic/acoustic emission sources in the rockmass structure for underground mining. *Eng Fract Mech* 2019;210:95–112.
- [5] Ma J, Dong LJ, Zhao GY, Li XB. Ground motions induced by mining seismic events with different focal mechanisms. *Int J Rock Mech Min Sci* 2019;116:99–110.
- [6] Ma J, Dong LJ, Zhao GY, Li XB. Qualitative method and case study for ground vibration of tunnels induced by fault-slip in underground mine. *Rock Mech Rock Eng* 2019;52(6):1887–901.
- [7] Dong LJ, Zou W, Sun DY, Tong XJ, Li XB, Shu WW. Some developments and new insights for microseismic/acoustic emission source localization. *Shock Vib* 2019;2019:1–15.
- [8] Dong LJ, Sun DY, Han GJ, Li XB, Hu QC, Shu L. Velocity-free localization of autonomous driverless vehicles in underground intelligent mines. *IEEE Trans Veh Technol*. In press.
- [9] Dong LJ, Tong XJ, Li XB, Zhou J, Wang SF, Liu B. Some developments and new insights of environmental problems and deep mining strategy for cleaner production in mines. *J Cleaner Prod* 2019;210:1562–78.
- [10] Feng GL, Feng XT, Chen BR, Xiao YX, Zhao ZN. Effects of structural planes on the microseismicity associated with rockburst development processes in deep tunnels of the Jinping-II Hydropower Station, China. *Tunn Undergr Space Technol* 2019;84:273–80.
- [11] Etgen J, Gray SH, Zhang Y. An overview of depth imaging in exploration geophysics. *Geophysics* 2009;74(6):WCA5–17.
- [12] Feng GL, Feng XT, Chen BR, Xiao YX, Yu Y. A microseismic method for dynamic warning of rockburst development processes in tunnels. *Rock Mech Rock Eng* 2015;48(5):2061–76.
- [13] Hu QC, Dong LJ. Acoustic emission source location and experimental verification for two-dimensional irregular complex structure. *IEEE Sens J* 2020;20(5):2679–91.
- [14] Virieux J, Operto S. An overview of full-waveform inversion in exploration geophysics. *Geophysics* 2009;74(6):WCC1–26.
- [15] Yi CP, Nordlund E, Zhang P, Warema S, Shirzadegan S. Numerical modeling for a simulated rockburst experiment using LS-DYNA. *Underground Space*. In press.
- [16] Otto R, Button EA, Bretterebehr H, Schwab P. The application of TRT—true reflection tomography—at the unterwald tunnel. *Felsbau* 2002;20(2):51–6.
- [17] Campbell G. Exploration geophysics of the Bushveld Complex in South Africa. *Lead Edge* 2011;30(6):622–38.
- [18] Yi CP, Johansson D, Greber J. Effects of *in-situ* stresses on the fracturing of rock by blasting. *Comput Geotechnol* 2018;104:321–30.
- [19] Dong LJ, Hu QC, Tong XJ, Liu YF. Velocity-free MS/AE source location method for three-dimensional hole-containing structures. *Engineering* 2020;6(7):827–34.
- [20] Baizhanov B, Katsuki D, Tutuncu AN, Mese AI. Experimental investigation of coupled geomechanical, acoustic, and permeability characterization of Berea sandstone using a novel true triaxial assembly. *Rock Mech Rock Eng* 2019;52(8):2491–503.
- [21] Bruning T, Karakus M, Nguyen GD, Goodchild D. Experimental study on the damage evolution of brittle rock under triaxial confinement with full circumferential strain control. *Rock Mech Rock Eng* 2018;51(11):3321–41.
- [22] Kim BC, Chen J, Kim JV. Relation between crack density and acoustic nonlinearity in thermally damaged sandstone. *Int J Rock Mech Min Sci* 2020;125:104171.
- [23] Rawlinson N, Fichtner A, Sambridge M, Young MK. Chapter one—seismic tomography and the assessment of uncertainty. *Adv Geophys* 2014;55:1–76.
- [24] Aben FM, Brantut N, Mitchell TM, David EC. Rupture energetics in crustal rock from laboratory-scale seismic tomography. *Geophys Res Lett* 2019;46(13):7337–44.
- [25] Behnia A, Chai HK, Yorikawa M, Momoki S, Terazawa M, Shiozani T. Integrated non-destructive assessment of concrete structures under flexure by acoustic emission and travel time tomography. *Constr Build Mater* 2014;67(Pt B):202–15.
- [26] Gupta IN. Seismic velocities in rock subjected to axial loading up to shear fracture. *J Geophys Res* 1973;78(29):6936–42.

- [27] Jansen DP, Carlson SR, Young RP, Hutchins DA. Ultrasonic imaging and acoustic emission monitoring of thermally induced microcracks in Lac du Bonnet granite. *J Geophys Res Solid Earth* 1993;98(B12):22231–43.
- [28] Nishizawa O, Lei XL. A numerical study on finding an optimum model in velocity tomography by using the extended information criterion. *Geophys Res Lett* 1995;22(10):1313–6.
- [29] Lei XL, Xue ZQ. Ultrasonic velocity and attenuation during CO<sub>2</sub> injection into water-saturated porous sandstone: measurements using difference seismic tomography. *Phys Earth Planet Inter* 2009;176(3–4):224–34.
- [30] Brantut N. Time-resolved tomography using acoustic emissions in the laboratory, and application to sandstone compaction. *Geophys J Int* 2018;213(3):2177–92.